Production of four-prong final states in photon-photon collisions

H. Aihara,[n] M. Alston-Garnjost,[a] R. E. Avery,[a] A. Barbaro-Galtieri,[a] A. R. Barker,[g] A. V. Barnes,[a] B. A. Barnett,[j] D. A. Bauer,[g] H.-U. Bengtsson,[d] D. L. Bintinger,[f] G. J. Bobbink,[h] T. S. Bolognese,[a] A. D. Bross,[a] C. D. Buchanan,[d] A. Buijs,[m] D. O. Caldwell,[g] A. R. Clark,[a] G. D. Cowan,[a] D. A. Crane,[j] O. I. Dahl,[a] K. A. Derby,[a] J. J. Eastman,[a] P. H. Eberhard,[a] T. K. Edberg,[a] A. M. Eisner,[c] R. Enomoto,[n] F. C. Erné,[m] T. Fujii,[n] J. W. Gary,[a] W. Gorn,[e] J. M. Hauptman,[i] W. Hofmann,[a] J. E. Huth,[a] J. Hylen,[j] T. Kamae,[n] H. S. Kaye,[a] K. H. Kees,[f] R. W. Kenney,[a] L. T. Kerth,[a] Winston Ko,[b] R. I. Koda,[d] R. R. Kofler,[k] K. K. Kwong,[e] R. L. Lander,[b] W. G. J. Langeveld,[e] J. G. Layter,[e] F. L. Linde,[m] C. S. Lindsey,[e] S. C. Loken,[a] A. Lu,[g] X-Q. Lu,[j] G. R. Lynch,[a] R. J. Madaras,[a] K. Maeshima,[b] B. D. Magnuson,[c] J. N. Marx,[a] G. E. Masek,[f] L. G. Mathis,[a] J. A. J. Matthews,[j] S. J. Maxfield,[k] S. O. Melnikoff,[e] E. S. Miller,[f] W. Moses,[a] R. R. McNeil,[b] P. Nemethy,[l] D. R. Nygren,[a] P. J. Oddone,[a] H. P. Paar,[m] D. A. Park,[d] S. K. Park,[i] D. E. Pellett,[b] M. Pripstein,[a] M. T. Ronan,[a] R. R. Ross,[a] F. R. Rouse,[a] K. A. Schwitkis,[g] J. C. Sens,[m] G. Shapiro,[a] M. D. Shapiro,[a] B. C. Shen,[e] W. E. Slater,[d] J. R. Smith,[b] J. S. Steinman,[d] M. L. Stevenson,[a] D. H. Stork,[d] M. G. Strauss,[d] M. K. Sullivan,[c] T. Takahashi,[n] J. R. Thompson,[f] N. Toge,[n] S. Toutounchi,[k] R. van Tyen,[a] B. van Uitert,[m] G. J. VanDalen,[e] R. F. van Daalen Wetters,[d] W. Vernon,[f] W. Wagner,[b] E. M. Wang,[a] Y. X. Wang,[g] M. R. Wayne,[d] W. A. Wenzel,[a] J. T. White,[f] M. C. S. Williams,[b] Z. R. Wolf,[a] H. Yamamoto,[a] S. J. Yellin,[g] C. Zeitlin,[b] and W-M. Zhang[j]

[a]*Lawrence Berkeley Laboratory, Berkeley, California 94720*
[b]*University of California, Davis, California 95616*
[c]*University of California Intercampus Institute for Research at Particle Accelerators, Stanford, California 94305*
[d]*University of California, Los Angeles, California 90024*
[e]*University of California, Riverside, California 92521*
[f]*University of California, San Diego, California 92093*
[g]*University of California, Santa Barbara, California 93106*
[h] *Carnegie-Mellon University, Pittsburgh, Pennsylvania 15213*
[i]*Ames Laboratory, Iowa State University, Ames, Iowa 50011*
[j]*Johns Hopkins University, Baltimore, Maryland 21218*
[k]*University of Massachusetts, Amherst, Massachusetts 01003*
[l]*New York University, New York, New York 10003*
[m]*National Institute for Nuclear and High Energy Physics, Amsterdam, The Netherlands*
[n]*University of Tokyo, Tokyo, Japan*
(TPC/Two-Gamma Collaboration)
(Received 27 February 1987)

Results are presented on the exclusive production of four-prong final states in photon-photon collisions from the TPC/Two-Gamma detector at the SLAC e^+e^- storage ring PEP. Measurement of dE/dx and momentum in the time-projection chamber (TPC) provides identification of the final states $2\pi^+2\pi^-$, $K^+K^-\pi^+\pi^-$, and $2K^+2K^-$. For two quasireal incident photons, both the $2\pi^+2\pi^-$ and $K^+K^-\pi^+\pi^-$ cross sections show a steep rise from threshold to a peak value, followed by a decrease at higher mass. Cross sections for the production of the final states $\rho^0\rho^0$, $\rho^0\pi^+\pi^-$, and $\phi\pi^+\pi^-$ are presented, together with upper limits for $\phi\rho^0$, $\phi\phi$, and $K^{*0}\bar{K}^{*0}$. The $\rho^0\rho^0$ contribution dominates the four-pion cross section at low masses, but falls to nearly zero above 2 GeV. Such behavior is inconsistent with expectations from vector dominance but can be accommodated by four-quark resonance models or by t-channel factorization. Angular distributions for the part of the data dominated by $\rho^0\rho^0$ final states are consistent with the production of $J^P=2^+$ or 0^+ resonances but also with isotropic (nonresonant) production. When one of the virtual photons has mass ($M_\gamma^2=-Q^2\neq 0$), the four-pion cross section is still dominated by $\rho^0\rho^0$ at low final-state masses $W_{\gamma\gamma}$ and by $2\pi^+2\pi^-$ at higher mass. Further, the dependence of the cross section on Q^2 becomes increasingly flat as $W_{\gamma\gamma}$ increases.

I. INTRODUCTION

The idea of vector-meson dominance has been used successfully in the past to describe the hadronic character of the photon.[1,2] Models such as these can be applied to photon-photon collisions to predict the production of neutral-vector-meson pairs such as $\rho^0\rho^0$, $\rho^0\phi$, $\phi\phi$, $\rho\omega$, etc. Of these, the pairs $\rho^0\rho^0$, $\rho^0\phi$, and $\phi\phi$ decay to

the all-charged four-prong final states $2\pi^+2\pi^-$, $K^+K^-\pi^+\pi^-$, and $2K^+2K^-$, which can be measured with a magnetic detector if sufficient particle identification is provided. In this paper we describe an analysis of these final states.

Since its first observation in 1980 by the TASSO Collaboration,[3] the reaction $\gamma\gamma \to \rho^0\rho^0$ has been extensively investigated.[4,5] The production cross section was found to exceed the vector-dominance-model (VDM) expectation by almost an order of magnitude near the $\rho^0\rho^0$ threshold. Similar enhancements have been found in the decay[6] $J/\psi \to \gamma\rho\rho$ and in inelastic antiproton scattering off deuterium,[7] $\bar{p}d \to \pi^-(2\pi^+2\pi^-)$. Interestingly, no enhancement has been found in the process $\gamma\gamma \to \rho^+\rho^-$, for which the JADE Collaboration has established preliminary upper limits.[8]

Several models have been proposed to explain the experimental data. In four-quark models,[9,10] isoscalar and isotensor resonances interfere destructively to suppress the $\rho^+\rho^-$ signal, while reproducing the $\rho^0\rho^0$ cross-section well. In a t-channel factorization approach, $\rho^0\rho^0$ cross sections are derived from photo- and electroproduction data.[11] Some perturbative-QCD model calculations have been made that are expected to be valid for high energies.[12,13] The predicted cross sections vary strongly depending on the model. The above models all predict the production of the final state $K^{*0}\bar{K}^{*0}$, in contrast with the VDM.

The analysis presented in this paper is based on data collected at an e^+e^- center-of-mass energy of 29 GeV using the SLAC e^+e^- storage ring PEP and the TPC/Two-Gamma facility.[14] The data were taken with two different time-projection-chamber (TPC) magnetic fields. The low-magnetic-field (4 kG) sample can be divided into an untagged data set with an integrated luminosity of 73 pb^{-1} (where the final-state e^+ and e^- are not detected) and a singly tagged data set of 50 pb^{-1} (where one final-state e^+ or e^-, the tag, is detected). Of the data collected with a higher magnetic field (13.2 kG), a singly tagged sample corresponding to 42 pb^{-1} has been analyzed.

II. APPARATUS

Since the TPC/Two-Gamma facility has been described previously,[15] only those properties that are of importance to this analysis will be discussed here. The equipment is shown in Fig. 1.

Starting from the interaction point, particles encounter as part of the central detector an inner pressure-vessel wall, the inner drift chamber (IDC), the time-projection chamber (TPC), the outer pressure-vessel wall, the magnet coil, the outer drift chamber (ODC), the hexagonal calorimeter, and three layers of iron and muon chambers. Particles emerging from the interaction region in a more forward direction with respect to the beam line, but still passing through the TPC, are detected in the pole-tip calorimeters and end-cap muon chambers. Still smaller angles were covered by the forward detector, consisting of a Čerenkov counter, a set of five planar drift chambers, a time-of-flight scintillator hodoscope, a calorimeter formed by an array of NaI crystals at small angles and a lead/scintillator-sandwich shower counter at larger angles, and finally three layers of drift chambers interspersed with iron for muon identification.

The time-projection chamber is a large drift chamber with the electric field parallel to the magnetic field, allowing very long drift distances. The chamber is two meters long with a diameter of two meters and covers about 97% of 4π solid angle: particles can be detected at angles as small as 250 mrad with respect to the beam line. A central membrane, perpendicular to the beam line, is kept at high voltage (50–75 kV) and provides, together with a series of equipotential rings, a uniform electric field parallel to the beam line. The two end planes are at ground potential. A charged particle traversing the detector volume ionizes the gas; ionization electrons drift along the electric field lines to the end planes where they are detected. The magnetic field substantially reduces the diffusion of the ionization electrons perpendicular to the drift direction by causing them to spiral around the electric field lines. The TPC is operat-

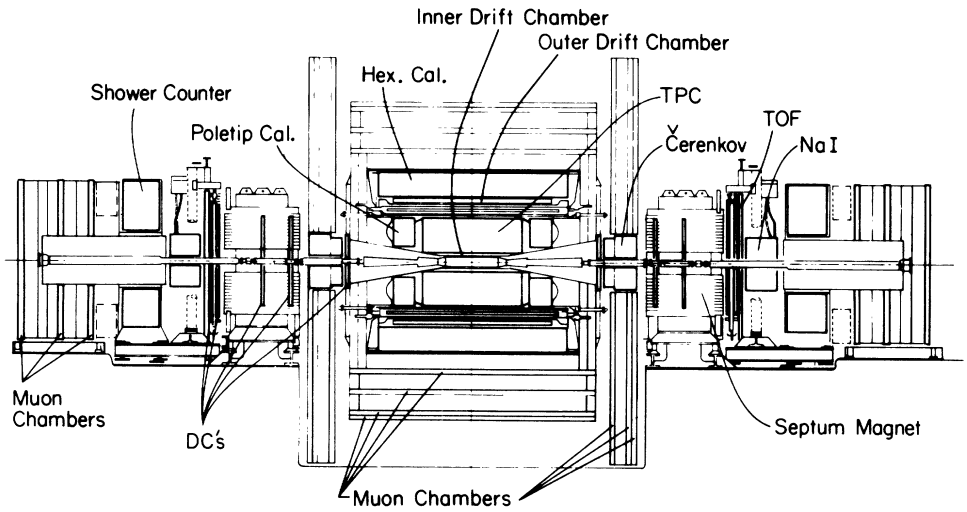

FIG. 1. The TPC/Two-Gamma detector.

ed with a gas mixture of 80% argon and 20% methane at 8.5 atm, corresponding to typically 200 ionization electrons per cm of track. The end planes are subdivided in six sectors, each sector having 183 proportional wires and 15 rows of segmented cathode pads. The pads are 7 mm$\times$7 mm and there are 1152 pads per sector. True three-dimensional coordinates can be derived from the time of arrival on the wire and the signals induced on the row of cathode pads under the proportional wire. Each pad and wire is connected to an individual electronics channel, consisting of a preamplifier, a shaping amplifier, a delay line (charge-coupled device) and a digitizer. From each channel, pulse height information to an accuracy of 1% and timing information to an accuracy of $\approx$20 ns are obtained. The pulse heights are directly proportional to the ionization energy loss of the detected particles. The lowest 65% of the samples provided by the 30–183 wires contributing to each track define the truncated mean dE/dx. A dE/dx resolution of 3.5% is achieved in this way.

The IDC is placed at the inner radius of the TPC in the same gas volume. It consists of four concentric layers of 60 sense wires each. Its polar angular coverage extends down to about 250 mrad with respect to the beam line. The total amount of material a particle encounters before reaching the TPC fiducial volume is equivalent to about 20% of a radiation length. Some changes in the detector hardware that were made at the time the superconducting coil was installed reduced the amount of material between the beam line and the TPC to about 15% of a radiation length.

The magnetic field for the low-field data was provided by a room-temperature solenoidal magnet ($\sim$1.3 radiation lengths) located between the outer pressure-vessel wall of the TPC and the ODC. It produced a nearly homogeneous magnetic field of 4 kG. This led to a momentum resolution at 90° of $(\sigma_p/p)^2 \approx (0.06)^2 + (0.035p)^2$, with p in GeV. For the more recent high-field data set a superconducting coil ($\sim$0.7 radiation lengths) was used with a magnetic field of 13.2 kG. The higher field and the addition of a gating system and a new field cage to reduce drift distortions resulted in a much-improved momentum resolution of $(\sigma_p/p)^2 \approx (0.015)^2 + (0.01p)^2$, again with p in GeV.

The ODC is located outside the magnet coil. It has three layers of drift cells with 216 wires per layer. The chamber consists of six modules that overlap, so that there are no gaps in azimuth. It covers polar angles starting from 38° and operators with the same gas as the TPC, but at atmospheric pressure.

The NaI electromagnetic shower detectors, each consisting of 60 hexagonal NaI(Tl) crystals, were used to detect final-state electrons in the angular range 22–90 mrad. Each crystal measures 6 in. apex to apex and is 20 in. long, corresponding to about 20 radiation lengths. Absolute energy calibrations to 0.3% were obtained by use of Bhabha events. An energy resolution of $\sigma_E/E = 1.0$–$1.5\,\%$ at 14.5 GeV was obtained. The position resolution was 5 mm rms (corresponding to 1 mrad angular resolution).

The small-angle spectrometers each also included a lead-scintillator shower counter, covering 100–180 mrad. Each unit consisted of 55 layers of lead sheets interspersed with scintillator strips for a total depth of about 18 radiation lengths. The energy resolution was $\sigma_E/E \approx 20\%/\sqrt{E}$ (E in GeV) and the spatial resolution $\approx$1 cm rms.

Each spectrometer also contained five forward drift chambers with a total of 15 wire planes and a septum magnet with $\int B\,dl \approx 2.6$ kG m. For the analysis presented here, this system was used primarily to ensure that tags were due to charged particles rather than photons.

The trigger for untagged events required at least two tracks in the TPC at a polar angle $\gtrsim 30°$ in different 60° sectors. The two tracks causing the trigger had to be pretriggered by the IDC and either the ODC (for track polar angles $\gtrsim 40°$) or the TPC (for angles $\lesssim 40°$).

The trigger for tagged events required the presence of an energy deposition of at least 2 GeV in the NaI or 8 GeV in the forward shower counter, in coincidence with at least one, more loosely defined, track in the TPC.

III. EVENT SELECTION AND PARTICLE IDENTIFICATION

Events were selected with exactly four well-measured charged prongs in the TPC coming from the vertex, having net charge zero. Events containing e^+e^- pairs due to photon conversions were rejected.

The measurement of energy loss (dE/dx) and momentum (p) in the TPC was used to identify each four-prong event. The measured values for each track were fitted to semiempirical curves of dE/dx vs p and a χ_i^2 was determined for the particle-species assumptions $i = e$, π, K, or p. A track was then said to be compatible with a species

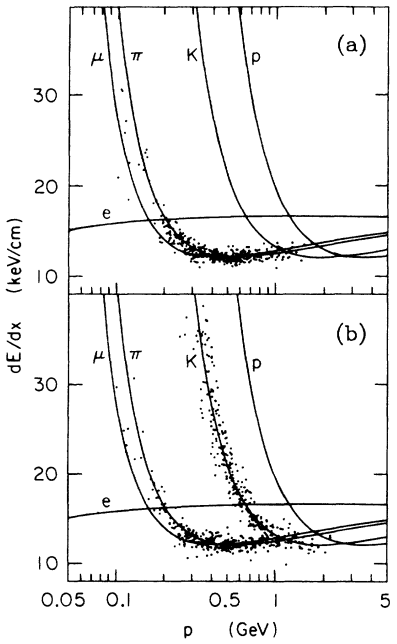

FIG. 2. The distribution of dE/dx vs momentum for the four prongs of (a) $2\pi^+2\pi^-$ and (b) $K^+K^-\pi^+\pi^-$ final states. Plot (a) shows only a small fraction of the events.

TABLE I. Number of events after all cuts, by final state.

Event type	Untagged events (73 pb^{-1})	Tagged events (92 pb^{-1})
$2\pi^+2\pi^-$	4637	992
$K^+K^-\pi^+\pi^-$	175	42
$2K^+2K^-$	2	0
Total	4814	1034

if the χ^2 for a particular fit was less than 8. The identification was called unambiguous if χ^2+4 for that hypothesis was less than the χ_i^2 of the other fits. For the $2\pi^+2\pi^-$ analysis all particles had to be compatible with the pion hypothesis, with one unambiguously identified as such. For the $K^+K^-\pi^+\pi^-$ analysis the K^+K^- ($\pi^+\pi^-$) pair had to consist of two oppositely charged particles, of which at least one was identified unambiguously as a kaon (pion), whereas the other had to be kaon (pion) compatible. For the $2K^+2K^-$ sample all particles had to be compatible with the kaon hypothesis and two particles with equal charge had to be unambiguously identified. The dE/dx is plotted versus momentum in Fig. 2 for the final states $2\pi^+2\pi^-$ and $K^+K^-\pi^+\pi^-$. The cleanliness of the figures is, of course, artificial because of the dE/dx selection criteria. They show, however, that the samples are not contaminated by other final states: such a contamination would lead to clustering of the data points around overlap regions.

All $K^+K^-\pi^+\pi^-$ and $2K^+2K^-$ candidates as well as a fraction of the $2\pi^+2\pi^-$ candidates were subjected to a visual scan in order to reject events with additional deposited energy in the calorimeters or extra unreconstructed tracks. For the untagged $2\pi^+2\pi^-$ sample, a requirement that $|\sum \mathbf{p}_\perp|$ is less than 200 MeV was found to be largely equivalent to the eye scan and was therefore imposed on the entire $2\pi^+2\pi^-$ sample. The $|\sum \mathbf{p}_\perp|$ cut on the $K^+K^-\pi^+\pi^-$ and $2K^+2K^-$ samples was <400 MeV. A minimum momentum was required for each particle: 100 MeV for pions and 200 MeV for kaons, with a minimum polar angle of $\theta \gtrsim 300$ mrad. A tagged event had one e^+ or e^- (the tag) with an energy $E \geq 4.0$ GeV in either the NaI or the shower counter. A cut of <200 MeV was imposed on the component of the total-transverse-momentum vector perpendicular to the lepton scattering plane, in addition to a standard $|\sum \mathbf{p}_\perp|$ cut of <400 MeV (including a tag in the NaI) or <800 MeV (including a tag in the shower counter). Events with evidence for additional charged or neutral tracks in the forward spectrometer were rejected.

The event samples are summarized in Table I. The total number of tagged events is about a factor of 5 smaller than that of untagged events.

IV. PARTICLE-PAIR SPECTRA, UNTAGGED DATA

A. Pair spectra in $2\pi^+2\pi^-$ events

The spectra of the invariant mass of pion pairs in $\gamma\gamma \to 2\pi^+2\pi^-$ events are shown in Figs. 3(a)–3(c), for three ranges of the total invariant mass $W_{\gamma\gamma}$. The first mass range (1.2–1.4 GeV) was chosen below, the second (1.6–2.0) above, the $\rho\rho$ threshold. The third mass range (2.4–3.6 GeV) was chosen in order to maximize the effect of potential contributions from charmonium final states. The opposite-sign combinations are shown as data points with four entries per event; the same sign combinations are shown as the histograms underneath, with two entries per event. The spectra for the mass ranges 1.6–2.0 GeV [Fig. 3(b)] and 2.4–3.6 GeV [Fig. 3(c)] clearly show evidence of ρ-meson production. The solid line in Fig. 3(b) represents a fit to the data of a relativistic Breit-Wigner form superimposed on a polynomial background. The mass and width obtained by this fit agree well with the nominal mass and width of the ρ meson.[16] A contribution from the $f_2(1270)$ is included in the fit shown in Fig. 3(c). In this fit, the peak positions and widths of the ρ^0 and f_2 were fixed at their nominal values. Since in Fig. 3(a) the mass range is below the threshold for $\rho^0\rho^0$ production, the ρ-signal is distorted. Figures 3(d)–3(j) show the correlation plots for the pair masses corresponding to the data in Figs. 3(a)–3(c). In Figs. 3(d)–3(f) the opposite sign combinations are plotted (two entries per events) and in Figs.

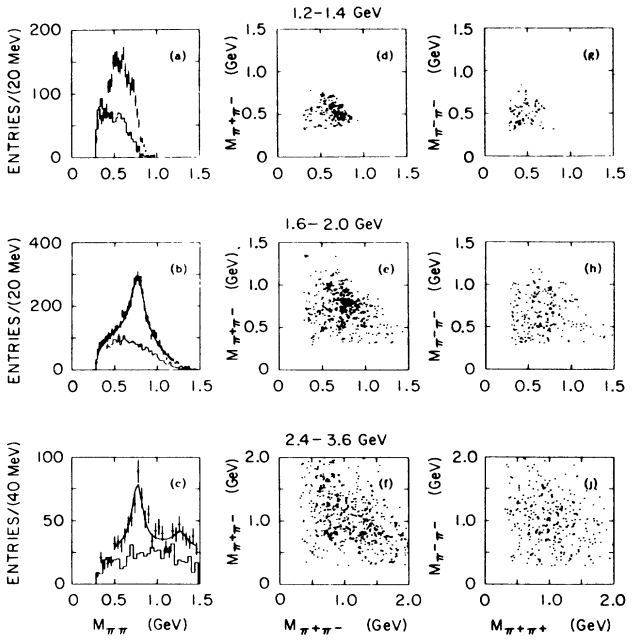

FIG. 3. The invariant-mass distributions of pion pairs in $\gamma\gamma \to 2\pi^+2\pi^-$ events for different ranges of $W_{\gamma\gamma}$. The data points with (statistical) errors in (a)–(c) are for opposite-sign pairs (four entries per event); the histograms are for the equal sign pairs (two entries per event). The curves in (b) and (c) are fits to the data of a Breit-Wigner resonance curve and a polynomial background. The correlation plots correspond to the histograms (d)–(f) showing the opposite-sign pairs (two entries per event), (g)–(h) the equal-sign pairs. Plots (d), (e), (g), and (h) contain a random 20% of the events. The $W_{\gamma\gamma}$ range is 1.2–1.4 GeV for the top row, 1.6–2.0 GeV for the middle row, and 2.4–3.6 GeV for the bottom row.

3(g)–3(j) the equal-sign combinations (one entry per event). The clustering in the opposite-sign correlation plots [Figs. 3(d) and 3(e)], which is absent in the equal-sign correlation plots [Figs. 3(g) and 3(h)], suggests the presence of a $\rho^0\rho^0$ final state. This has been observed earlier by the TASSO (Ref. 3) Collaboration, which has attempted to extract the fractions of $\rho^0\rho^0$, $\rho^0\pi^+\pi^-$, and $2\pi^+2\pi^-$ events using likelihood fits. It should be noted that two factors may affect the results of these fits. First, the $\pi^+\pi^-$ system in the $\rho^0\pi^+\pi^-$ component must be in a relative $P,F,\ldots$ wave in order to achieve the correct charge conjugation for the overall state.[9] This angular momentum will reduce the available phase space for low masses, leading to an overestimate of the $\rho^0\rho^0$ contribution below threshold. Second, the processes $\gamma\gamma\to a_1(1270)\pi$, $\gamma\gamma\to f_2(1270)\pi^+\pi^-$, and $\gamma\gamma\to f_2(1270)$ may contribute to the four-pion channel. The first of these reactions would lead to events of the type $\gamma\gamma\to\rho^0\pi^+\pi^-$, the others to $\gamma\gamma\to 2\pi^+2\pi^-$. The $f_2(1270)\pi^+\pi^-$ state is not subject to P-wave suppression.

It is clear that an incoherent mixture of isotropic $\rho^0\rho^0$, $\rho^0\pi^+\pi^-$, and nonresonant $2\pi^+2\pi^-$ events may not exhaustively describe the data. A more complete model of $2\pi^+2\pi^-$ production is, at present, not available. We have, therefore, limited the scope of this analysis of the particle fractions to a check on the results obtained by the TASSO Collaboration, using the same model and fitting method. In this model, an ansatz is made to describe the differential production cross section:

$$\frac{d\sigma_i}{d\xi}=\frac{(2\pi)^4}{4\sqrt{X}}R_4(W_{\gamma\gamma},\xi)\,|\,g_i'(W_{\gamma\gamma})g_i(\xi)\,|^2$$

$$=C(W_{\gamma\gamma})R_4(W_{\gamma\gamma},\xi)\,|\,g_i(\xi)\,|^2\ . \tag{4.1}$$

Here $R_4(W_{\gamma\gamma},\xi)$ is the four-particle phase-space density, $\sqrt{X}=W_{\gamma\gamma}^2/2$, and $g_i'(W_{\gamma\gamma})$ and $g_i(\xi)$ represent the $W_{\gamma\gamma}$ and the ξ-dependent parts of the matrix element for the process i, respectively. The $W_{\gamma\gamma}$ dependence of the matrix element and the flux factors are absorbed in $C(W_{\gamma\gamma})$, taken to be constant in each 200-MeV bin of $W_{\gamma\gamma}$. In untagged four-pion events there are twelve possible coordinates describing four particles in three-momentum space. One is determined by the value of $W_{\gamma\gamma}$, three are determined by conservation of momentum, and a fifth is redundant because the four-pion system is invariant under rotation around the $\gamma\gamma$ axis. For the remaining seven independent coordinates we have chosen

$$\xi=(m_{12}^2,m_{34}^2,\theta_{12},\theta_{\pi_{12}},\phi_{\pi_{12}}\theta_{\pi_{34}},\phi_{\pi_{34}})\ .$$

The symbol m_{ab} stands for the invariant mass of the pion pair (a,b), where the pions are numbered $\pi_1^+\pi_2^-\pi_3^+\pi_4^-$. The angle θ_{12} is the polar angle of the particle pair (1,2) with respect to the $\gamma\gamma$ axis in the $\gamma\gamma$ center of mass. The angles $\theta_{\pi_{ab}}$ and $\phi_{\pi_{ab}}$ are the polar and azimuthal angles of one of the pions with respect to the $\gamma\gamma$ axis in the center-of-mass system of the pair.

The phase-space density is taken to be identical for all processes: the distinction between the processes is made through the matrix element g_i, where i stands for $\rho^0\rho^0$, $\rho^0\pi^+\pi^-$, or $2\pi^+2\pi^-$. Here we only consider isotropic production and decay of these final states and, therefore, $g_i(\xi)$ is independent of the angular coordinates and only determined by m_{12} and m_{34}. But since we have two pairs of identical bosons in our $2\pi^+2\pi^-$ final state, we must construct a matrix element symmetric under interchange of two pions with the same charge. The functions satisfying these requirements are

$$g_{2\pi^+2\pi^-}=\text{const}\ ,$$

$$g_{\rho^0\pi^+\pi^-}\propto\tfrac{1}{2}[B_\rho(m_{12})+B_\rho(m_{34})+B_\rho(m_{14})+B_\rho(m_{23})]\ ,$$

and (4.2)

$$g_{\rho^0\rho^0}\propto\frac{1}{\sqrt{2}}[B_\rho(m_{12})B_\rho(m_{34})+B_\rho(m_{14})B_\rho(m_{23})]\ .$$

In the Breit-Wigner amplitude B_ρ an energy-dependent width was chosen for the ρ:

$$B_\rho(m)=\frac{(m_\rho\Gamma m/p^*)^{1/2}}{\pi(m_\rho^2-m^2-im_\rho\Gamma)} \tag{4.3}$$

with

$$\Gamma=\Gamma_\rho\left[\frac{p^*}{p_0^*}\right]^3\frac{2p_0^{*2}}{p_0^{*2}+p^{*2}}\ , \tag{4.4}$$

$$p^*=\tfrac{1}{2}(m^2-4m_\pi^2)^{1/2},\quad p_0^*=\tfrac{1}{2}(m_\rho^2-4m_\pi^2)^{1/2}\ ,$$

and[16]

$$m_\rho=770\ \text{MeV},\quad \Gamma_\rho=153\ \text{MeV}\ .$$

In Monte Carlo calculations, events were generated with the final state distributed according to phase space and the mass dependence of the $\gamma\gamma$ luminosity function[17] (i.e., assuming $d\sigma_i/d\xi=1$). The appropriate weight $|\,g_i(\xi)\,|^2$ was later assigned to the accepted events. The masses were generated uniformly over the region $m_{12}>2m_\pi$, $m_{34}>2m_\pi$, $m_{12}+m_{34}<W_{\gamma\gamma}$; the event configuration was obtained after a hit-and-miss selection on $R_4(W_{\gamma\gamma},\xi)$.

The generated events were subjected to a detector simulation, which included multiple scattering, nuclear interactions, energy loss in the detector material, decay of final-state particles, trigger efficiency, and detector resolution. The acceptance curves obtained by this calculation are shown as a function of $W_{\gamma\gamma}$ for $\rho^0\rho^0$ and $2\pi^+2\pi^-$ in Figs. 4(a) and 4(b) and are seen to be quite similar. The acceptance of $\rho^0\pi^+\pi^-$ lies between the two. For the systematic uncertainties (shown as shaded areas) the following sources were included: the effect of the kinematic cuts on the acceptance of the events (from 20% at low mass to 15% at high mass), the loss of particles due to nuclear interactions in the inner detector region (15%), the dE/dx particle identification (8%), the calculation of the trigger efficiency (25–10 %), and the e^+e^- luminosity (10%).

To extract the fractions of observed events[18] λ_i

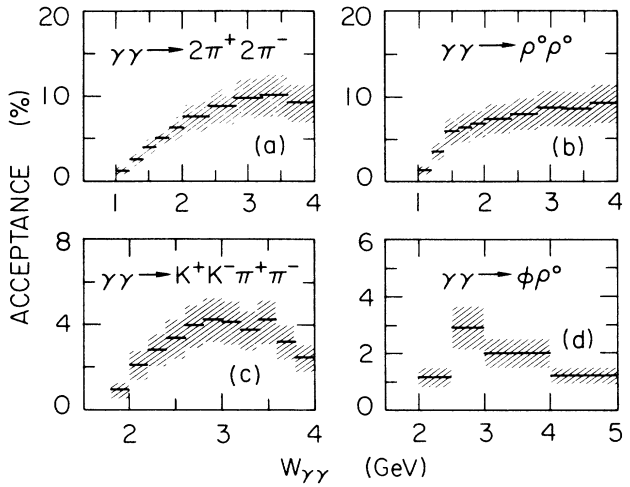

FIG. 4. The detection and reconstruction efficiency as a function of the $\gamma\gamma$ invariant mass $W_{\gamma\gamma}$ for the processes (a) $\gamma\gamma \to 2\pi^+2\pi^-$, (b) $\gamma\gamma \to \rho^0\rho^0$, (c) $\gamma\gamma \to K^+K^-\pi^+\pi^-$, and (d) $\gamma\gamma \to \phi\rho^0$. The shaded areas indicate the extent of the systematic errors.

($i = \rho^0\rho^0$, $\rho^0\pi^+\pi^-$, $\pi^+\pi^-\pi^+\pi^-$) from the data, each event was assigned values for the probabilities P_i that the event resulted from the process i. Then the probability for the whole data sample was maximized using the maximum-likelihood procedure described in Ref. 3. The likelihood function is defined by

$$\Lambda = \prod_n \sum_i \lambda_i P_i(\xi_n) \tag{4.5}$$

with the constraint

$$\sum_i \lambda_i = 1 \ . \tag{4.6}$$

The product runs over all events. The quantity $P_i(\xi_n)$ is the normalized probability for the accepted event n with measured variables ξ_n to be produced by the process i:

$$P_i(\xi_n) = \frac{A(\xi_n) d\sigma_i(\xi_n)/d\xi}{\int A(\xi) d\sigma_i(\xi)} \ , \tag{4.7}$$

where $A(\xi)$ is the acceptance for an event with phase-space variables ξ. The fit then requires maximization of the quantity

$$\sum_n \left[\ln \left[\sum_i \lambda_i \frac{|g_i(\xi_n)|^2}{\int A(\xi) d\sigma_i(\xi)} \right] - \sum_i \lambda_i \right] , \tag{4.8}$$

where Eq. (4.1) was used. The integrals are evaluated using a Monte Carlo procedure.

The results are shown in Fig. 5 as a function of $W_{\gamma\gamma}$. The errors in the fractions were determined by the fitting procedure. Clearly, however, the model used here is a very simple one. It does not include mutual interference effects between the three final states considered and also includes only the simplest possible orbital angular-momentum configurations. The resulting possible model dependence of the procedure together with the systematic uncertainties of the acceptance calculations led us to assign an estimated systematic error of 0.2 to the fractions.

We conclude that the $2\pi^+2\pi^-$ final state is predominantly $\rho^0\rho^0$ at masses below the nominal $\rho^0\rho^0$ threshold, but that the $\rho^0\rho^0$ component diminishes rapidly with increasing mass and nearly vanishes above 2 GeV. The $\rho^0\pi^+\pi^-$ component shows the opposite behavior: it is compatible with zero below threshold, and rises above threshold until it approximately equals the nonresonant component, which has a roughly constant level of $\approx 40\%$ throughout the mass range. Our results agree well with those from the TASSO Collaboration,[3] also shown in Fig. 5.

An attempt was made to include the process $\gamma\gamma \to a_1(1270)\pi$ in the fit. It was found, however, that the $a_1\pi$ final state is very similar to the $\rho\pi^+\pi^-$ final state. Therefore, fits including both final states are unstable.

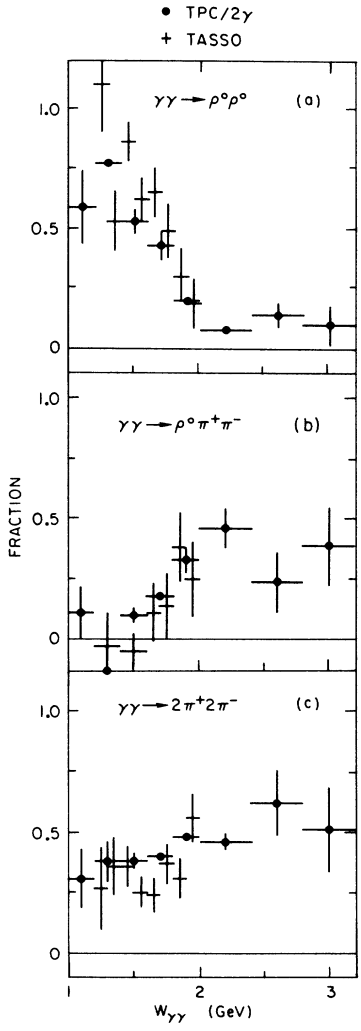

FIG. 5. The fractions of the observed $2\pi^+2\pi^-$ events contributed by the processes $\rho^0\rho^0$, $\rho^0\pi^+\pi^-$, and $2\pi^+2\pi^-$ as a function of $W_{\gamma\gamma}$. The results from the TASSO Collaboration (Ref. 3) are included for comparison. The error bars represent the uncertainty as determined by the fitting procedure.

B. Pair spectra in $K^+K^-\pi^+\pi^-$ events

The distributions of the two-particle invariant-mass spectra of untagged $\gamma\gamma \to K^+K^-\pi^+\pi^-$ events are shown in Fig. 6. The K^+K^- spectrum, Fig. 6(a), rises from zero at threshold to a maximum at ≈ 1.3 GeV as the detection efficiency and available phase space increase and then fall due to the decreasing photon-photon flux at higher masses. The peak just above threshold contains 11 events with a K^+K^- invariant mass below 1040 MeV and is attributed to the production of ϕ mesons. There is an estimated background of two events from nonresonant $K^+K^-\pi^+\pi^-$. Figure 6(b) shows the $\pi^+\pi^-$ spectrum. The shaded histogram shows only the events containing a ϕ. In neither histogram is there strong evidence of ρ^0 meson production. We conclude that we observe the reaction $\gamma\gamma \to \phi\pi^+\pi^-$, but not $\gamma\gamma \to \phi\rho^0$.

The $\phi\pi^+\pi^-$ events were subsequently removed from the data sample. Figure 6(c) shows the correlation between the $K^+\pi^-$ and the $K^-\pi^+$ masses of the remaining events. There is a concentration in the lower-left corner of the plot with two faint bands extending upwards and sideways, approximately symmetric under charge reversal. The sum of the projections on either axis of this scatter plot is shown as data points in Fig. 6(d). The histogram in this figure shows the distribution for the equal-sign $K\pi$ pairs. Since both distributions have two entries per event, the latter histogram was divided by 2. There is clearly evidence for the production of $K^{*0}(892)$. The solid line through the data points represents a fit to a Breit-Wigner resonance curve on a polynomial background. The results of this fit agree with the resonance parameters of the $K^{*0}(892)$. We conclude that we observe the production of K^{*0} mesons.

The contributions of the final states $K^{*0}\bar{K}^{*0}$, $K^{*0}K^{\pm}\pi^{\mp}$, and nonresonant $K^+K^-\pi^+\pi^-$ to the $K^+K^-\pi^+\pi^-$ sample were estimated by fitting Monte Carlo–generated event distributions of the three processes to the correlation plot, Fig. 6(c). The Monte Carlo events were generated with a constant matrix element and a weight was assigned to each event to reproduce the $W_{\gamma\gamma}$ distribution of the data. The efficiencies for the three processes were found to be equal to within 5%; for the $K^+K^-\pi^+\pi^-$ final state the efficiency is shown as a function of $W_{\gamma\gamma}$ in Fig. 4(c). The systematic uncertainty (shown as shaded area) is the same as for the $2\pi^+2\pi^-$ data in corresponding mass ranges with the exception of the error due to the dE/dx particle identification, which is more complicated for the case of kaons: it ranges from 14% at low mass to 8% at higher mass. The fractions, averaged over the mass range of 1.8–4.0 GeV, then are

$$K^+K^-\pi^+\pi^-\text{: } (47\pm15)\% ,$$

$$K^{*0}K\pi\text{: } (44\pm14)\% ,$$

$$K^{*0}\bar{K}^{*0}\text{: } (9\pm7)\% .$$

The errors shown are the quadratic sum of the statistical and systematic errors. The latter were obtained by varying the bin size in the fitting procedure and recording the variations in the fractions.

The contribution from the vector-vector state $K^{*0}\bar{K}^{*0}$ is compatible with zero, and the event sample can therefore be described with equal contributions of $K^{*0}K^{\pm}\pi^{\mp}$ and nonresonant $K^+K^-\pi^+\pi^-$. Some of the results on this final state were published earlier.[19]

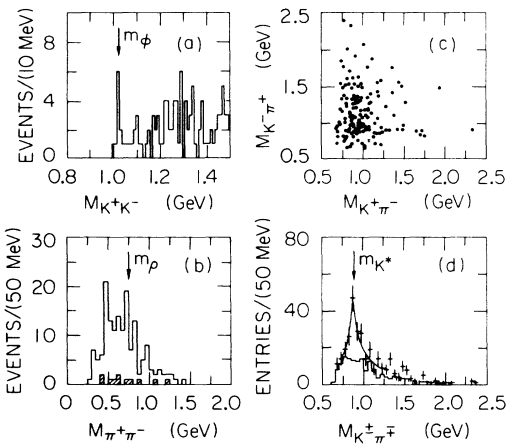

FIG. 6. Two-particle invariant-mass distributions in the final $K^+K^-\pi^+\pi^-$ sample: (a) K^+K^-; (b) $\pi^+\pi^-$, where the shaded histogram denotes masses recoiling against a ϕ meson; (c) $K^+\pi^-$ vs $K^-\pi^+$; (d) the projection of (c) on both axes, $K^\pm\pi^\mp$ (data points with statistical errors) and $K^\pm\pi^\pm$ (histogram). The $\phi\pi^+\pi^-$ events were excluded from the distributions of (c) and (d). The curve in (d) represents a fit of a Breit-Wigner resonance curve on a polynomial background.

C. Events with four kaons

We find two events with four kaons. One of them is of the type $\phi\phi$, the other of the type ϕK^+K^-. The presence of three ϕ mesons in two $2K^+2K^-$ events is remarkable in comparison with the 11 ϕ mesons in the 175 $K^+K^-\pi^+\pi^-$ events. However, it is consistent with the large number of ρ mesons observed in the $2\pi^+2\pi^-$ data. The invariant mass of the ϕK^+K^- event is 3.06 ± 0.07 GeV and that of the $\phi\phi$ event is 5.1 ± 0.2 GeV.

V. PRODUCTION CROSS SECTIONS, UNTAGGED DATA

A. Backgrounds

As was stated before, all events from the processes $\gamma\gamma \to K^+K^-\pi^+\pi^-$ and $2K^+2K^-$ were scanned by eye, and badly measured events and events with additional photons were rejected. After the scan, the $|\sum \mathbf{p}_\perp|^2$ distribution for each process agreed well enough with the Monte Carlo prediction so that no further background from other than exclusive four-prong final states was subtracted. However, estimates of the number of incorrectly identified events were made for each process by submitting Monte Carlo samples of $2\pi^+2\pi^-$ and $K^+K^-\pi^+\pi^-$ events to the analysis programs for the other processes. In this procedure we find that the $K^+K^-\pi^+\pi^-$ sample may be contaminated by 13 events

(7%) from the $2\pi^+2\pi^-$ final state. The two $2K^+2K^-$ events are likely to be free of background.

The $|\sum \mathbf{p}_\perp|^2$ distribution for the $2\pi^+2\pi^-$ data, shown in Fig. 7, peaks at low $|\sum \mathbf{p}_\perp|^2$, but tends towards a constant level at large $|\sum \mathbf{p}_\perp|^2$. A Monte Carlo simulation for the $|\sum \mathbf{p}_\perp|^2$ distribution does not reproduce the data very well, and we conclude that a substantial background from events with undetected particles is still present in the sample. In order to determine this background, events of the types $\pi^+\pi^+\pi^+\pi^-$ and $\pi^-\pi^-\pi^+\pi^-$ were selected and subjected to the same analysis without the charge-conservation requirement. The $|\sum \mathbf{p}_\perp|^2$ distribution for these events is flat, due to the fact that at least two particles must be missing. This distribution is shown in Fig. 7 as the lower histogram. It was taken to represent the background to the $2\pi^+2\pi^-$ data, after normalization to the difference between the data and Monte Carlo distributions for $2\pi^+2\pi^-$ events at $|\sum \mathbf{p}_\perp|^2 > 0.25$ GeV^2. The sum of the resulting background and the Monte Carlo simulation is shown in Fig. 7 as the upper histogram. Reasonable agreement is obtained. The procedure was carried out in several bins of $W_{\gamma\gamma}$. After the $|\sum \mathbf{p}_\perp|$ cut, a contamination of 13% is then found in the mass bin from 1.0 to 1.2 GeV, decreasing to 11% between 1.2 and 2.0 GeV, and rising again to 15% at 4.0 GeV. The $2\pi^+2\pi^-$ and $\rho^0\rho^0$ cross sections given in the following section have been corrected for this background, assuming that the background contributes equally to either process. As a check, part of the sample was subjected to an eye scan. It was found that the eye scan leads to essentially the same results.

B. Cross sections

The cross sections are calculated as a function of the invariant mass $W_{\gamma\gamma}$ of the two-photon system by dividing the raw-event distribution by the acceptance (Fig. 4) and by the $\gamma\gamma$ luminosity function.[17] The calculated cross sections are compiled in Fig. 8.

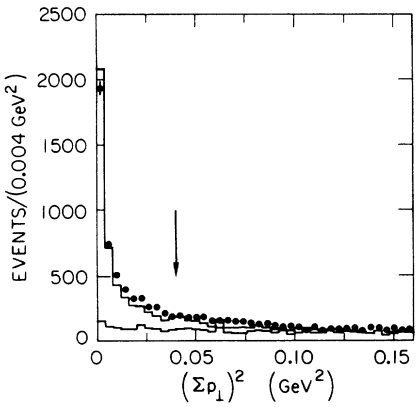

FIG. 7. The $|\sum \mathbf{p}_\perp|^2$ distribution for untagged $2\pi^+2\pi^-$ events. The histogram through the data points is the sum of a Monte Carlo simulation of the $2\pi^+2\pi^-$ final state and background as determined from $\pi^+\pi^+\pi^+\pi^-$ and $\pi^-\pi^-\pi^-\pi^+$ data (lower histogram). The arrow indicates where the cut was applied.

In Fig. 8(a) the production cross section for the process $\gamma\gamma \to 2\pi^+2\pi^-$ is shown with statistical errors only. All four-pion events were used in this calculation, regardless of ρ^0 content. The acceptance curve for nonresonant $2\pi^+2\pi^-$ production [Fig. 4(a)] was used; however, those for $\rho^0\rho^0$ [Fig. 4(b)] and $\rho^0\pi^+\pi^-$ are very similar. The uncertainty in the cross section is dominated by the systematic uncertainty in the acceptance (see Fig. 4). In Fig. 8(b) the $\rho^0\rho^0$ component of the $2\pi^+2\pi^-$ sample is shown. It is obtained from Fig. 8(a) by multiplication with the $\rho^0\rho^0$ fraction, Fig. 5(a). Since the uncertainty in the fraction determination is not correlated with the one in the acceptance calculation, the errors are added in quadrature to give the error in the $\rho^0\rho^0$ cross section. Also shown are the results from the TASSO Collaboration,[3] which are in good agreement with our data. Thus we confirm the observation of a broad threshold enhancement in the $\gamma\gamma \to \rho^0\rho^0$ channel. In Fig. 8(c) the cross section for $\gamma\gamma \to \rho^0\rho^0$ is compared to the models by Alexander *et al.*[11] and Achasov *et al.*[9] Also shown are data points for the $\gamma\gamma \to \pi^+\pi^-\pi^0\pi^0$ final state as measured by the JADE Collaboration,[8] together with the prediction of Achasov *et al.* The JADE points were obtained by selecting all $\pi^+\pi^-\pi^0\pi^0$ events compatible with the $\rho^+\rho^-$ assumption and can therefore be interpreted as upper limits for $\gamma\gamma \to \rho^+\rho^-$.

A similar phenomenon is observed in the

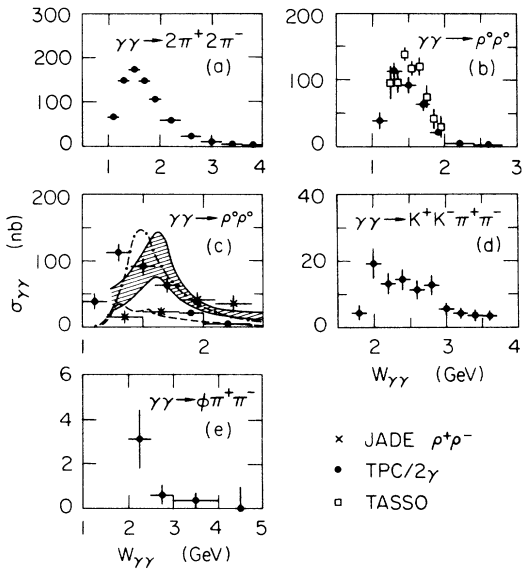

FIG. 8. The production cross section as a function of $W_{\gamma\gamma}$ for the processes (a) $\gamma\gamma \to 2\pi^+2\pi^-$ (including $\rho^0\rho^0$) and (b) $\gamma\gamma \to \rho^0\rho^0$. The TASSO results (Ref. 3) on $\gamma\gamma \to \rho^0\rho^0$ are included in (b) for comparison. In (c) the $\gamma\gamma \to \rho^0\rho^0$ cross section is compared to models by Alexander *et al.* (Ref. 11) (shaded area) and Achasov *et al.* (Ref. 9) (dotted-dashed line). Also displayed are the upper-limit results from the JADE Collaboration (Ref. 8) for the $\gamma\gamma \to \rho^+\rho^-$ final state together with Achasov's prediction (dashed line). The production cross sections for the processes $\gamma\gamma \to K^+K^-\pi^+\pi^-$ and $\gamma\gamma \to \phi\pi^+\pi^-$ are shown in (d) and (e), respectively. The error bars in (a), (d), and (e) are statistical; those in (b) and (c) include the errors in the $\rho^0\rho^0$ fractions (as determined by the fits).

$K^+K^-\pi^+\pi^-$ channel, plotted in Fig. 8(d). The cross section for $\gamma\gamma\to K^+K^-\pi^+\pi^-$ (excluding $\phi\pi^+\pi^-$) rises from threshold to a maximum value of ≈ 20 nb around $W_{\gamma\gamma}=2$ GeV, and then decreases slowly with rising $W_{\gamma\gamma}$. The width of the threshold enhancement in $K^+K^-\pi^+\pi^-$ is of the order of 1 GeV, significantly larger than in the $2\pi^+2\pi^-$ case. The systematic errors are of about the same magnitude as the statistical ones shown. The $\phi\pi^+\pi^-$ component is shown in Fig. 8(e). The $\phi\pi^+\pi^-$ cross section is ≈ 3 nb between 2.0 and 2.4 GeV, and then drops rapidly to zero. The acceptance curve for $\phi\rho^0$ [Fig. 4(d)] was used to calculate the cross section; statistics dominate the uncertainty in the measurement.

The mass dependence of the square of the matrix element $|g'(W_{\gamma\gamma})|^2$ [see Eq. (4.1)] can be calculated from the cross section by dividing by the nonresonant phase space and flux factors. The result is shown in Fig. 9 for both the $2\pi^+2\pi^-$ and $K^+K^-\pi^+\pi^-$ data, with the same normalization for both reactions. It is interesting to note that with phase-space effects removed there is no compelling indication left of any resonant behavior. The $2\pi^+2\pi^-$ and $K^+K^-\pi^+\pi^-$ data have a very similar mass dependence, suggesting similar underlying production mechanisms at these masses.

Upper limits (95% confidence level) on the cross sections for $\phi\rho^0$, $\phi\phi$, and $K^{*0}\bar{K}^{*0}$ production are shown as a function of $W_{\gamma\gamma}$ in Figs. 10(a)–10(c). The branching ratios of ϕ to K^+K^- and K^{*0} to $K^\pm\pi^\mp$ are accounted for in these figures. Because of the large width of the ρ meson, the $\phi\pi^+\pi^-$ events were weighted with a Breit-Wigner resonance curve with proper normalization. A similar weighting procedure was used for the $K^{*0}\bar{K}^{*0}$ events. The curves shown in Figs. 10(a)–10(c) are the predictions by Achasov *et al.*[9] for four-quark resonant states. Our upper limits do not contradict the four-quark models.

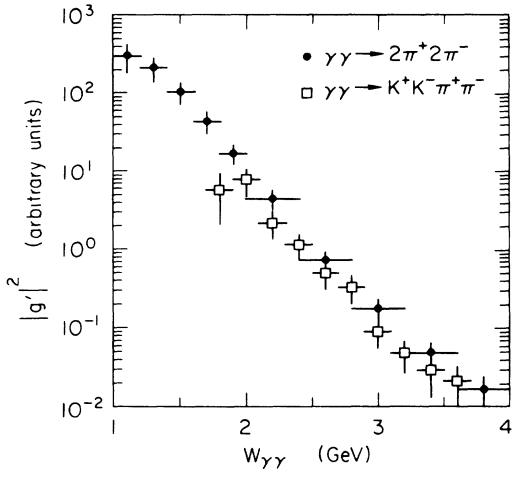

FIG. 9. The measured value of the square of the matrix element $|g'|^2$ as a function of $W_{\gamma\gamma}$ for the processes $\gamma\gamma\to 2\pi^+2\pi^-$ (including $\rho^0\pi^+\pi^-$ and $\rho^0\rho^0$) and $\gamma\gamma\to K^+K^-\pi^+\pi^-$. The error bars include the systematic errors.

C. Upper limits on η_c formation

The $2\pi^+2\pi^-$ and $K^+K^-\pi^+\pi^-$ cross sections above were used to extract 95%-C.L. upper limits on the formation of the η_c meson. In a fit, a Gaussian was used with a width of 75 MeV (determined by the mass resolution) at the nominal mass of the η_c, 2980 MeV, superimposed on a polynomial background. For the $2\pi^+2\pi^-$ data we then obtain an upper limit

$$\Gamma_{\gamma\gamma\to\eta_c}B_{\eta_c\to 2\pi^+2\pi^-}<0.9\ \text{keV}\ , \tag{5.1}$$

and, for the $K^+K^-\pi^+\pi^-$ data,

$$\Gamma_{\gamma\gamma\to\eta_c}B_{\eta_c\to K^+K^-\pi^+\pi^-}<0.8\ \text{keV}\ . \tag{5.2}$$

For the $\phi\phi$ final state there are no events at the η_c mass, leading to an upper limit of

$$\Gamma_{\gamma\gamma\to\eta_c}B_{\eta_c\to\phi\phi}<0.34\ \text{keV}\ . \tag{5.3}$$

Using the branching ratios measured by the Mark III Collaboration[20] of $(1.3\pm0.6)\%$, $(2.1\pm0.3)\%$, and $(0.8\pm0.3)\%$, respectively, we compute upper limits of 69, 37, and 43 keV for the $\gamma\gamma$ width of the η_c. The errors in

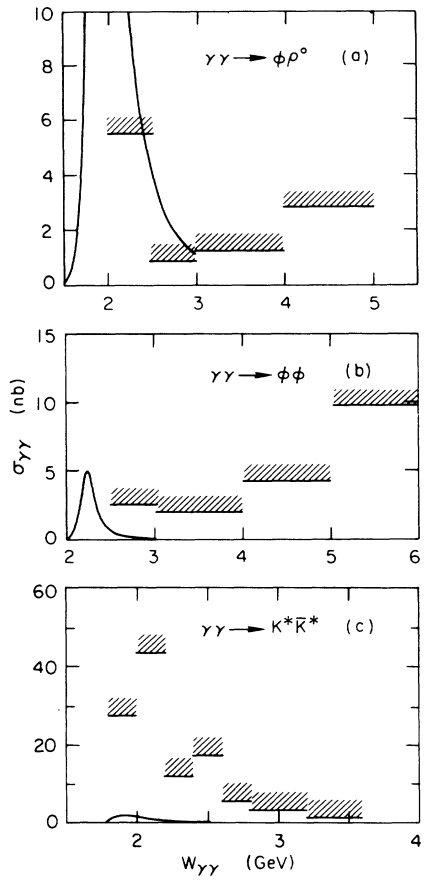

FIG. 10. Upper limits (95% confidence level) on the production cross sections for (a) $\gamma\gamma\to\phi\rho^0$, (b) $\phi\phi$, (c) $K^{*0}\bar{K}^{*0}$, as a function of $W_{\gamma\gamma}$. The curves in (a)–(c) are predictions for four-quark states by Achasov *et al.* (Ref. 9).

the branching ratios were not taken into account in the upper limit. These should be compared to the measurement of the PLUTO Collaboration[21] for the process $\gamma\gamma \to \eta_c \to K_S^0 K^{\pm}\pi^{\mp}$, from which a value for the $\gamma\gamma$ width of the η_c of 33 ± 20 keV can be derived, using a branching ratio[20] of $1.5\pm0.6\%$.

VI. ANGULAR CORRELATIONS

To determine the spin-parity of the $\rho^0\rho^0$ part of the untagged $2\pi^+2\pi^-$ data, two approaches were followed.

In Fig. 11 the experimental angular distributions are shown. Because the $\rho\rho$ contribution is maximal around 1.5 GeV, the mass range was restricted to 1.4–1.6 GeV. The plotted points represent two entries for each event [four for Fig. (b)] weighted by the $\rho^0\rho^0$ matrix element squared $|g_{\rho\rho}|^2$ of Eq. (4.2). This procedure accounts for the fact that one is unable to distinguish $\rho^0\rho^0$ from $\rho^0\pi^+\pi^-$ or $2\pi^+2\pi^-$ events and the fact that it is not possible to identify which $\pi^+\pi^-$ combinations within an event originated from the actual ρ decays. The background from $2\pi^+2\pi^-$ and $\rho^0\pi^+\pi^-$ is estimated to be reduced by this procedure to a level of 10–15 %. The four curves are calculations of the angular distributions obtained by weighting phase-space Monte Carlo events with $|g_{\rho\rho}|^2$ times the angular distribution for the four possible spin-parity states $J^P=0^+$, 0^-, 2^+, and 2^-, corrected for acceptance (for $J^P=2^+$ a 1:6 ratio was used for the helicity 0 to helicity 2 contributions).

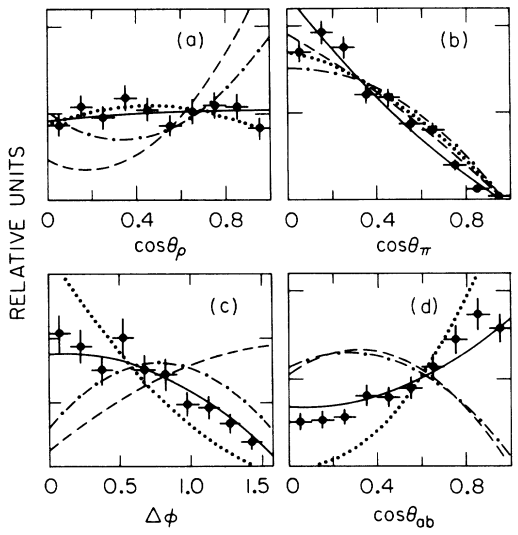

FIG. 11. Angular distributions of the $2\pi^+2\pi^-$ sample for the mass range 1.4–1.6 GeV. (a) $\cos\theta_\rho$, the cosine of the polar angle of the ρ^0 with respect to the $\gamma\gamma$ axis in the $\gamma\gamma$ center of mass. (b) $\cos\theta_\pi$, the cosine of the polar angle of the pions with respect to the $\gamma\gamma$ axis in the ρ center of mass (the Adair frame). (c) $\Delta\phi$, the angle between the decay planes of the two ρ's in the $\gamma\gamma$ center of mass. (d) $\cos\theta_{ab}$, the normalized dot product between the decay directions taken in the ρ rest frames with parallel axes (physically meaningful only in the nonrelativistic limit). The lines represent acceptance-corrected calculations for the four spin-parities 0^+ (dotted), 2^+ (solid), 0^- (dotted-dashed), and 2^- (dashed). Only statistical errors are included in the data points.

Displayed are $\cos\theta_\rho$, the cosine of the polar angle of the ρ^0 with respect to the $\gamma\gamma$ axis in the $\gamma\gamma$ center of mass [Fig. 11(a)], $\cos\theta_\pi$, the cosine of the polar angle of the pions with respect to the $\gamma\gamma$ axis in the ρ center-of-mass (Adair) frame [Fig. 11(b)], $\Delta\phi$, the angle between the decay planes of the two ρ's in the $\gamma\gamma$ center of mass [Fig. 11(c)], and $\cos\theta_{ab}$, the normalized dot product between the decay directions taken in the ρ rest frames with parallel axes (physically meaningful only in the nonrelativistic limit) [Fig. 11(d)]. Clearly, the data are not consistent with the negative-parity curves, confirming a conclusion reached by the TASSO Collaboration.[3] The data follow the $J^P=2^+$ curve very well, but some contribution from 0^+ cannot be excluded. The $\cos\theta_\rho$ distribution is shown for four mass regions in Fig. 12. Below 2 GeV the angular distribution remains flat as expected for 0^+ and 2^+ $\rho\rho$ production; at higher masses, where the $\rho\rho$ contribution is small, it peaks in the forward direction.

In a second approach, a six-parameter fit was performed in which the contribution of $g_{\rho\rho}$ of Eq. (4.2) was replaced by four contributions $g_{\rho\rho}\Psi(J^P)$, where $\Psi(J^P)$ is the angular distribution for spin-parity J^P, and $J^P=0^+$, 0^-, 2^+, and 2^-. The results confirm our earlier conclusion that the data are inconsistent with the negative-parity states. The data do not, however, allow a more specific determination of the ratio $0^+/2^+$. It should be observed, that the 2^+ angular distributions are indistinguishable from isotropy within the statistical errors. Like TASSO (Ref. 3) we find that the sum of the $\rho^0\rho^0$ cross sections from this fit is lower than the one obtained from the three-parameter fit. It is difficult to ascertain the significance of this discrepancy.

Finally, the angular distributions of the $K^+K^-\pi^+\pi^-$ final state were studied. In Fig. 13(a) the cosine of the angle of each neutral $K\pi$ pair with respect to the $\gamma\gamma$ axis is shown, and in Fig. 13(b) the cosine of the angle between the kaon direction and the $\gamma\gamma$ axis in the $K\pi$ center of mass. The histograms in the same figures represent the result of an isotropic phase-space Monte

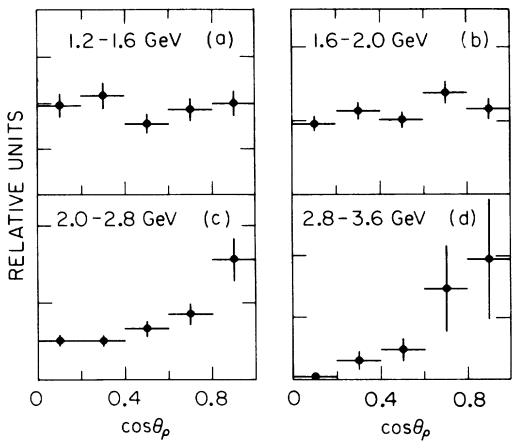

FIG. 12. The $\cos\theta_\rho$ distribution in four different regions of $W_{\gamma\gamma}$ (statistical errors only).

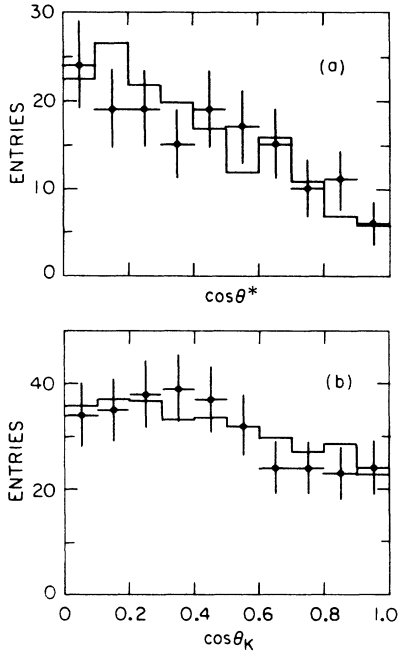

FIG. 13. (a) Event distribution of untagged $K^+K^-\pi^+\pi^-$ events as a function of the angle θ^* of one neutral $K\pi$ pair with respect to the $\gamma\gamma$ axis in the $\gamma\gamma$ center of mass (one entry per event). (b) Event distribution of the angle of the kaons with respect to the $\gamma\gamma$ axis in the center of mass of the corresponding neutral $K\pi$ pair (two entries per event). The crosses represent data points with statistical errors; the histograms are the result of a Monte Carlo simulation of isotropic $K^+K^-\pi^+\pi^-$ production.

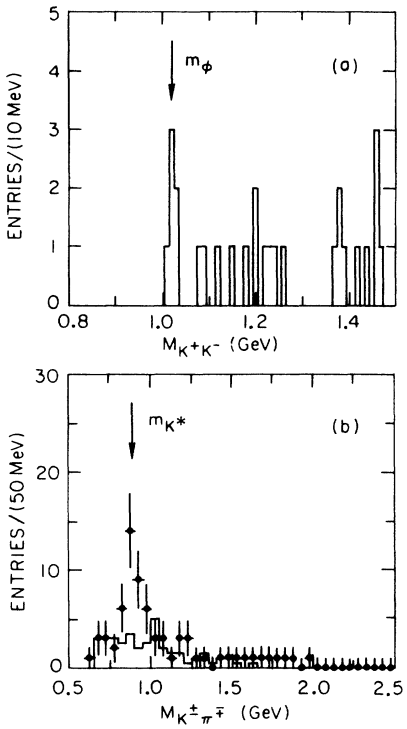

FIG. 14. Two-particle invariant-mass distributions in the tagged $K^+K^-\pi^+\pi^-$ sample: (a) K^+K^-, (b) $K^\pm\pi^\mp$ (data points with statistical errors) and $K^\pm\pi^\pm$ (histogram). The $\phi\pi^+\pi^-$ events were excluded from the distributions of (b).

Carlo calculation of the $K^+K^-\pi^+\pi^-$ final state. The data are clearly compatible with this Monte Carlo result.

VII. THE TAGGED DATA SAMPLES

Events of the types $2\pi^+2\pi^-$ and $K^+K^-\pi^+\pi^-$ were selected in which one of the two final-state leptons (the tag) was detected in the forward spectrometer. The selection criteria were described in Sec. III.

Figure 14(a) shows the K^+K^- spectrum in the $K^+K^-\pi^+\pi^-$ final state. Six events are compatible with $\phi\pi^+\pi^-$. The $\pi^+\pi^-$ mass spectrum does not show any structure and is therefore not shown here. After removing these six events we show in Fig. 14(b) the opposite-sign $K\pi$ mass spectrum as data points; the histogram represents the same-sign combinations divided by 2, as in Fig. 6. In spite of the limited statistics, a $K^*(892)$ enhancement is visible.

The magnitude of the $\rho^0\rho^0$ component of the $2\pi^+2\pi^-$ data as a function of $W_{\gamma\gamma}$ was established, as for the untagged data, by a maximum-likelihood fit, in two bins of $Q^2=-q^2$ (q is the four-momentum of the tagged photon) and five bins of $W_{\gamma\gamma}$. The results are shown in Table II. The errors are the ones determined by the fitting procedure. As stated earlier, the systematic error due to model dependence and acceptance variations is estimated to be of the order of 0.2. The general trend of the fractions was found to be preserved as Q^2 increases. Consequently, the Q^2 distribution of the $2\pi^+2\pi^-$ sample as a whole was determined without separating the fractions.

For the calculation of the cross sections, the efficiency

TABLE II. The fraction of observed $2\pi^+2\pi^-$ events attributed to $\rho^0\rho^0$ production as a function of Q^2. The errors are determined by the fitting procedure. An estimated systematic error of 0.2 is due to acceptance differences between the processes and model dependence of the procedure.

$W_{\gamma\gamma}$ (GeV)	$Q^2\approx 0$	$0.1<Q^2<0.5$ GeV^2	$Q^2>0.5$ GeV^2
1.2–1.4	0.77±0.02	0.67±0.18	0.46±0.37
1.4–1.6	0.53±0.05	0.77±0.13	0.67±0.29
1.6–2.0	0.31±0.06	0.25±0.20	0.22±0.12
2.0–2.8	0.11±0.05	−0.05±0.11	−0.01±0.16

was determined in bins of both $W_{\gamma\gamma}$ and Q^2. It was assumed that the backgrounds are the same as for the untagged data (see Sec. V A). The background-subtracted cross section for the $2\pi^+2\pi^-$ final state is plotted as a function of Q^2 in Fig. 15, in four bins of $W_{\gamma\gamma}$. All results were calculated using the transverse-transverse luminosity function only.[17] At high Q^2 a contribution is expected from the scalar-transverse cross section as well. What is plotted is therefore the effective cross section $\sigma_{TT}+\epsilon\sigma_{ST}$ with ϵ the photon polarization parameter. The errors on the $Q^2\neq 0$ GeV^2 data points are statistical only. The systematic error is slightly lower than for the untagged data because the trigger efficiency for the tagged data has a very small uncertainty. The data point at $Q^2\approx 0$ GeV^2 of each distribution is the result from the untagged data sample; its error includes the relative systematic error between the tagged and untagged samples.

The data do not fall off as steeply as a ρ-pole form factor squared, shown as the solid line in each figure, especially at higher mass. This is reasonable, since a contribution can be expected from the formation of charmonium states η_c, χ_0, and χ_2. The Q^2 dependence of the formation cross section of these states is expected to behave like a J/ψ-pole form factor squared,[22] which is represented by the dashed curves. Both are normalized to the cross section at $Q^2\approx 0$ GeV^2. Neither curve fits the data very well at any value of $W_{\gamma\gamma}$. However, in each mass range a linear combination of the two form

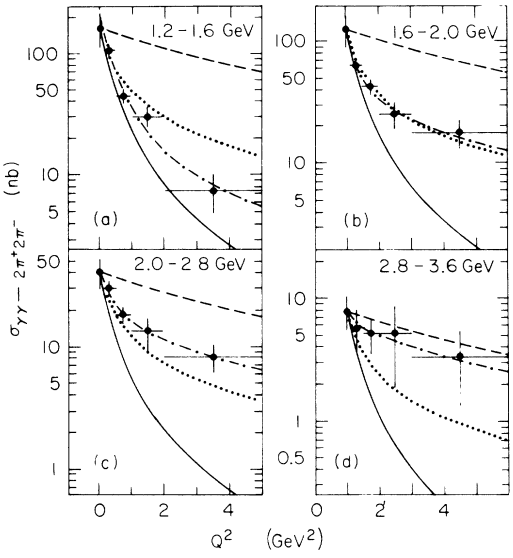

FIG. 15. The cross section for the process $\gamma\gamma\to 2\pi^+2\pi^-$ (including $\rho^0\pi^+\pi^-$ and $\rho^0\rho^0$) as a function of Q^2 in four bins of $W_{\gamma\gamma}$ as indicated. The solid lines represent the ρ-pole form factor, the dashed lines the J/ψ-pole form factor, and dotted lines the form factor expected from the generalized vector-meson-dominance model, all normalized to the first data point. The dotted-dashed lines give the best fit of a linear combination of the ρ-pole and J/ψ-pole form factors. For the $Q^2\neq 0$ data points only statistical errors are shown; for the $Q^2\approx 0$ point a relative systematic error was added in quadrature.

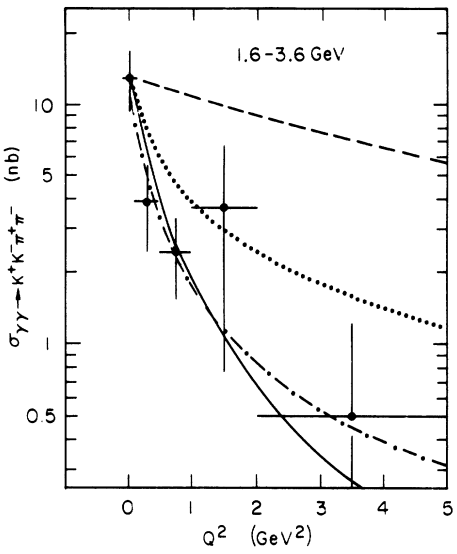

FIG. 16. The cross section for the process $\gamma\gamma\to K^+K^-\pi^+\pi^-$ (including $K^{*0}K\pi$ and $K^{*0}\bar{K}^{*0}$) as a function of Q^2. The curves and errors are as defined in Fig. 15.

factors can be found that agrees well with the data, as indicated by the dotted-dashed line. The ρ-pole form factor is dominant at low masses, but towards higher masses the J/ψ-pole contribution increases, suggesting the formation of $c\bar{c}$ states at these masses. On the other hand, a rather flat Q^2 dependence is also expected[23] from QCD for $\gamma\gamma\to\pi^0\pi^0$ and, hence, likely for $\gamma\gamma\to\rho^0\rho^0$.

For comparison, the dotted lines in Fig. 15 show the Q^2 dependence from the generalized vector-meson-dominance model (model II of Ref. 2).

The Q^2 dependence of the $\gamma\gamma\to K^+K^-\pi^+\pi^-$ cross section is shown in Fig. 16 for the entire measured mass range. The curves in this figure are analogous to the ones in Fig. 15. The cross section decreases rapidly with Q^2.

VIII. CONCLUSIONS

We have measured four-prong final states consisting of charged pions and kaons. The $2\pi^+2\pi^-$ events come from the final states $\rho^0\rho^0$ and $\rho^0\pi^+\pi^-$ and nonresonant $2\pi^+2\pi^-$. There is a strong $\rho^0\rho^0$ component at low $W_{\gamma\gamma}$, even below the nominal $\rho\rho$ threshold. This $\rho^0\rho^0$ component is consistent with a spin-parity of predominantly 0^+ and 2^+, but also with isotropic production. The $K^+K^-\pi^+\pi^-$ sample consists of $\phi\pi^+\pi^-$, $K^{*0}K\pi$ and nonresonant $K^+K^-\pi^+\pi^-$. The general feature of both the $2\pi^+2\pi^-$ and $K^+K^-\pi^+\pi^-$ final states is that the cross sections rise steeply from threshold to a peak value (about 180 nb for the $2\pi^+2\pi^-$ data versus about 20 nb for the $K^+K^-\pi^+\pi^-$ data) at about 0.5 GeV above threshold, and decrease at higher masses. This behavior is in contradiction with simple vector-meson-dominance models, but is more or less described by both the four-quark models[9] and the t-channel factorization models.[11]

The fractions of $\rho^0\rho^0$, $\rho^0\pi^+\pi^-$, and nonresonant

$2\pi^+2\pi^-$ in the tagged $2\pi^+2\pi^-$ data are similar to those in the untagged data. The Q^2 dependence of the $2\pi^+2\pi^-$ cross section itself falls off somewhat more slowly than a ρ-pole form factor at low mass and becomes even flatter at higher masses.

Two events of the type $\gamma\gamma \to 2K^+2K^-$ were found, one of which is identified as $\phi\phi$, the other as ϕK^+K^-.

In the untagged data, upper limits were established for the formation of the η_c meson.

ACKNOWLEDGMENTS

We acknowledge the efforts of the PEP staff and the engineers, programmers, and technicians of the collaborating institutions. This work was supported in part by the U.S. Department of Energy, the National Science Foundation, the Joint Japan–United States Collaboration in High Energy Physics and the Foundation for Fundamental Research on Matter in the Netherlands.

[1]J. J. Sakurai, Ann. Phys. (N.Y.) **11**, 1 (1960); J. J. Sakurai, Phys. Rev. Lett. **22**, 981 (1969).

[2]J. J. Sakurai and D. Schildknecht, Phys. Lett. **40B**, 121 (1972).

[3]TASSO Collaboration, R. Brandelik *et al.*, Phys. Lett. **97B**, 448 (1980); TASSO Collaboration, M. Althoff *et al.*, Z. Phys. C **16**, 13 (1982); **32**, 11 (1986).

[4]CELLO Collaboration, H.-J. Behrend *et al.*, Z. Phys. C **21**, 205 (1984).

[5]Mark II Collaboration, D. L. Burke, *et al.*, Phys. Lett. **103B**, 153 (1981).

[6]Mark III Collaboration, R. M. Baltrusaitis *et al.*, Phys. Rev. D **33**, 1222 (1986).

[7]D. Bridges *et al.*, Phys. Rev. Lett. **56**, 211 (1986); **56**, 215 (1986).

[8]H. Kolanoski, in *Proceedings of the 5th International Colloquium on $\gamma\gamma$ Interactions,* Aachen, edited by Ch. Berger (Lecture Notes in Physics, Vol. 191) (Springer, Berlin, 1983), p. 175.

[9]N. N. Achasov, S. A. Devyanin, and G. N. Shestakov, Phys. Lett. **108B**, 134 (1982); Z. Phys. C **16**, 55 (1982); *ibid.* **27**, 99 (1985).

[10]B.-A. Li and K.-F. Liu, Phys. Lett. **118B**, 435 (1982); Phys. Rev. Lett. **51**, 1510 (1983).

[11]G. Alexander, U. Maor, and P. G. Williams, Phys. Rev. D **26**, 1198 (1982); G. Alexander, A. Levy, and U. Maor, Z. Phys. C **30**, 65 (1986).

[12]S. J. Brodsky and G. P. Lepage, Phys. Rev. D **24**, 1808 (1981).

[13]V. I. Chernyak and I. R. Zhitnitsky, Nucl. Phys. **B222**, 382 (1983).

[14]More details can be found in A. Buijs, Ph.D. thesis, State University, Utrecht, The Netherlands, 1987.

[15]TPC Collaboration, H. Aihara *et al.*, IEEE Trans. Nucl. Sci. **NS-30**, 63 (1983); **NS-30**, 67 (1983); **NS-30**, 76 (1983); **NS-30**, 117 (1983); **NS-30**, 153 (1983); **NS-30**, 162 (1983); Two-Gamma Collaboration, M. P. Cain *et al.*, Phys. Lett. **147B**, 232 (1984).

[16]Particle Data Group, M. Aguilar-Benitez *et al.*, Phys. Lett. **170B**, 1 (1986).

[17]V. M. Budnev, I. F. Ginzburg, G. V. Meledin, and V. G. Serbo, Phys. Rep. **15C**, 181 (1975); G. Bonneau, M. Gourdin, and F. Martin, Nucl. Phys. **B54**, 573 (1973).

[18]Note that these observed fractions are identical to fractions of produced events if the acceptances for the processes $\rho^0\rho^0$, $\rho^0\pi^+\pi^-$, and $2\pi^+2\pi^-$ are the same (see Fig. 4).

[19]TPC/Two-Gamma Collaboration, H. Aihara *et al.*, Phys. Rev. Lett. **54**, 2564 (1985).

[20]Mark III Collaboration, R. M. Baltrusaitis *et al.*, Phys. Rev. D **33**, 629 (1986).

[21]PLUTO Collaboration, Ch. Berger *et al.*, Phys. Lett. **167B**, 120 (1986).

[22]F. C. Erné, in *Proceedings of the VIth International Workshop on Photon-Photon Collisions,* Granlibakken, Lake Tahoe, edited by R. L. Lander, (World Scientific, Singapore, 1985).

[23]J. F. Gunion, D. Millers, and K. Sparks, Phys. Rev. D **33**, 689 (1986).

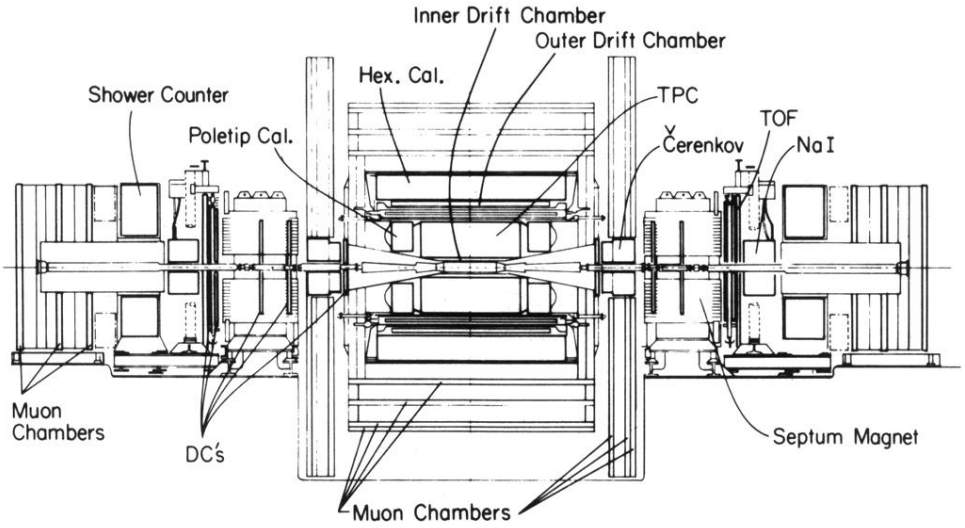

FIG. 1. The TPC/Two-Gamma detector.